Crystallographic orientation dependence of hydride precipitation in commercial pure titanium

Qian Wang[a,b], Shun Xu [c,*], Jean-Sébastien Lecomte [a,b], Christophe Schuman [a,b,**], Laurent Peltier [a,b], Xiao Shen [d], Wenwen Song [d]

[a] Laboratoire d'Etude des Microstructures et de Mécanique des Matériaux (LEM3), Université de Lorraine, CNRS, Arts et Métiers ParisTech, Metz , France

[b] Laboratory of Excellence on Design of Alloy Metals for low-mAss Structures (DAMAS), Université de Lorraine, France

[c] Mechanical and Materials Engineering, University of Nebraska-Lincoln, Lincoln, NE 68588, USA

[d] Steel Institute (IEHK), RWTH Aachen University, Intzestraße 1, 52072, Aachen, Germany

*Corresponding author.

**Corresponding author.

E-mail addresses: shunxufamily@gmail.com (Shun Xu),

christophe.schuman@univ-lorraine.fr (Christophe Schuman).

Abstract

Ti and its alloys have a variety of applications in aerospace industry and medical implants. The formation of hydride has been used in biomedical areas and can significantly influence the mechanical performance of materials. In this work, we investigate the orientation dependence of hydride precipitation in commercially pure titanium via interrupted in-situ electron backscatter diffraction (EBSD) measurements. The results reveal that hydrides during hydrogen charging at room temperature exhibit two types of orientation relationships with α-titanium, i.e., $\{0001\}_\alpha//\{1\bar{1}1\}_\delta$ $<1\bar{2}10>_\alpha//<110>_\delta$ with interface plane $\{10\bar{1}3\}_\alpha//\{1\bar{1}0\}_\delta$ (B-type), and $\{0001\}_\alpha//\{001\}_\delta$ $<1\bar{2}10>_\alpha//<110>_\delta$ with interface plane $\{10\bar{1}0\}_\alpha//\{1\bar{1}0\}_\delta$ (P-type). Significant orientation dependence of hydride precipitation is observed, especially when $\{10\bar{1}3\}$, $\{10\bar{1}0\}$, $\{0001\}$ or $\{11\bar{2}0\}$ planes of the parent grains are parallel to the diffusion surface. The displacement gradient tensor based accommodation shows that the orientation

1

dependence is attributed to the strain relaxation of hydride transition. Three types of hydride platelets are characterized: parallel hydride platelets (Type I), crossed hydride platelets (Type II) and clustered hydride platelets (Type III). The multiple morphologies of hydride platelets resulting from the hydride variant selection and interaction are dependent on the crystal orientation of the matrix.

Keywords: Titanium; Titanium hydride; Crystal orientation; Variant; EBSD

1. Introduction

Besides the superior properties, including fatigue-allowable strength, high thermal stability, good biocompatibility and excellent corrosion resistance [1], Ti and its alloys also possess high capability of storing large amounts of hydrogen by forming stable hydrides with moderate formation enthalpies [2]. A common dilemma is that the formation of the hydride precipitation results in hydrogen embrittlement and cleavage in front of a growing crack [3-5], which reduces the plasticity and fracture stress. As a result, the mechanical performance of the material is damaged. Morlet et al. [6] and Troiano [7] propose that hydrogen adsorbed at the crack tip can reduce the cohesive strength in lattice and surface energy of crack propagation. It is demonstrated that hydride can also be regarded as a plastic carrier. Carpenter et al. [8] point out that the dilatation misfit produced by formation of hydride platelet leads to the emission of dislocations. Chen et al. characterized the interaction between plastic deformation and hydrides [9, 10]. At certain volume fraction of hydrogen, the grain refinement associated with the introduction of deformation twins can improve mechanical properties including ultimate compression strength, word hardening rate and dislocation storage [11].

Crystal orientation is an important factor for determining the hydride precipitation in alloys. Zirconium alloys benefit from a huge literature because these metals are mainly used in the nuclear industry due to their low neutron absorption, good mechanical properties and excellent high-temperature corrosion resistance. The embrittlement induced by hydrogen limits their performance. Since there are a lot of similarities between Zr and Ti alloys (quasi-equal c/a, texture, etc) and no much work is available associated with the characterization and mechanical properties on titanium alloys under hydrogen environment, we got inspired by the existing work on zirconium alloys. Long et al. [12] examined the microstructure of a hydride blister grown in a Zircaloy-4 specimen, indicating that crystal orientation of α-Zr can affect the area fraction and the morphology of hydrides with different orientation relationships (ORs), but less preferential growth of hydrides in the parent grains with c-axis away from the normal direction to the plate is still unclear, which may be attributed to the complication of stress sources in the blister. The stress state is another important factor that can strongly affect the formation of hydride. Sharma et al [13] applied stress during the formation of hydride precipitation. The interface planes of the hydride platelets prefer normal to the direction of the external stress, which significantly increases the degree of embrittlement in Zr-2.5%Nb alloy.

Han et al. [14] proposed a micromechanical phase-field model for the formation and transition of the δ-hydrides stacking structure in Zr. The results suggest that hydride grows by repetitive nucleation, growth and coarsening near the pre-existing hydride platelet. The applied stress can transform the orientation of macro-hydride stacking structure through shifting the energetically favored nucleation site on the pre-existing hydride [14]. Besides, the external stress can decreases the critical nucleation energy of the grain boundary (GB) normal to the stress direction and further induce hydride nucleation in it [15].

Stress-induced hydride nucleation can be tuned through GB energy and texture adjustment, since the nucleation of hydride is governed by combined effect of grain boundary and orientation [15]. Indeed, grain boundary is a preferential site for hydride nucleation and most of hydrides are found at grain boundaries in the fine grain Zircaloy-4 [16]. There are higher proportion of intragranular hydrides in the large grain sample than in the fine sample [16]. However, the orientation of parent α-grain can not only influence the completeness of hydride transformation, but also the orientation relationship [12]. Thus, the research of grain orientation effect on hydride precipitation has more profound significance.

Three different Ti hydride phases have been observed so far, including metastable γ-hydride (TiH, face-centered tetragonal (FCT), $c/a > 1$), stable δ-hydride (TiH$_x$, $1.5 < x < 1.99$, face-centered cubic (FCC)) and ε-hydride (TiH$_2$, FCT, $c/a < 1$)) [17–21]. The δ phase is the most prevalent hydride phase and the formation mechanism is of particular interest. The distribution of δ phase hydride and hydride-matrix ORs in Ti and Zr alloys has been studied through electron backscatter diffraction (EBSD) based microstructural characterization [12,15,16,22–25]. Most of the work is focused on the hydride nucleated near grain boundaries instead of within the grains. The dependence of intragranular hydrides on grain orientations needs to be revealed as well as the morphology character and the interaction of intragranular hydrides, which will shed new light on hydride study of HCP metals and provide useful industrial application potentials.

The aim of this study is to investigate the relationship between crystal orientation of parent grains and α-Ti / δ-hydride transition in HCP titanium. Interrupted in-situ EBSD was performed to characterize the microstructural evolution before and after hydrogen charging. The dependence of the FCC hydride on the grain orientations was revealed. Anisotropic strain associated with hydride phase transformation was calculated to address the orientation dependence of hydride precipitation. The characterization of hydride platelets has been performed to explore the variant selection and the interaction between hydrides.

4

2. Methodology

In the current work, the material used was rolled commercially pure titanium T40 (ASTM grade 2) sheet with the thickness of 1.5 mm, which was first annealed under high vacuum condition at 800 ^{o}C for 3 h. The obtained material was fully recrystallized with an average grain size of ~30 μm and the texture is a typical split basal texture with basal pole oriented ±20° away from the normal direction (ND) of the sheet towards the transverse direction (TD). Then, hydrogens were introduced into the specimens through concentration gradient by an electrolytic method [24,25]. Hydrides precipitated when the hydrogens were supersaturated in the matrix. A platinum anode of cylindrical shape was used and the specimen was located in the center of the electrolytic cell as illustrated in Fig. 1. The specimens were charged with hydrogen in an electrolyte consisting of 1/3 volume phosphoric acid (85 wt%) and 2/3 volume glycerin (85 wt%) [26] under an applied current density of 2 kA/m^2 for 168 h. Enough hydrides can precipitate on the diffusion surface and the sample is not over-corroded under this condition. A hydrogen concentration of 123 wt ppm was measured by thermal desorption analysis (TDA) at the Welding and Joining Institute (ISF) of the RWTH Aachen University using the analyzer G8 GALILEO (Bruker, Billerica, USA).

To obtain diffusion surfaces with different textures, two sets of samples are prepared, i.e., hydrogen diffusion direction is along the normal direction of the rolled titanium sheet and along the rolling direction. The former set is designated as Sample A and the latter one as Sample B. Interrupted in-situ microstructural observation before and after hydrogen charging was performed by EBSD measurements. After grinding with SiC papers of grits from 1200$^{\#}$ to 2400$^{\#}$, electrolytic polishing was performed on the diffusion surfaces of Sample A and Sample B using a solution of 10 vol% perchloric acid in methanol at 35 V 5 ^{o}C for 5 s for initial orientation detection. After that, hydrogen charging was performed and the microstructure of hydride layer can be examined directly under Scanning Electron Microscopy (SEM) and EBSD. In addition, to observe the microstructure of hydride platelets under the covered hydride layer, another sample was prepared by only mechanical polishing and was hydrogenated with normal direction parallel to diffusion direction like Sample A. After hydriding, it was electropolished for 1 s at 30 V for microstructural characterization of hydride platelets. The diffusion surface for hydriding with certain roughness can accelerate hydrogen diffusion, which makes sure that enough hydride platelets can be observed after electrolytic polishing. Especially, it is difficult to accurately distinguish multiple hydride phases (FCC and FCT) by EBSD. Thus, only FCC δ-hydride, the most prevalent hydride

phase, was chosen as indexed phase during EBSD measurements on the hydrogen-charged samples for determining the orientation relationship between the hydride precipitation and the parent grain.

Microstructure characterization was performed using JSM 6490 SEM and JEOL 6500F field emission gun microscopy equipped with an EBSD camera. The Aztec software package (Oxford Instruments) was employed for data acquisition. Forward Scattered Detectors (FSD) in JSM 6490 SEM was used to obtain the morphology of hydride platelet. To save the characterization time and obtain enough information for statistics, JSM 6490 SEM was used to make EBSD measurements in large area at a step size of 0.5 μm. Specifically, EBSD patterns were acquired on a JEOL 6500F field emission gun for obtaining more detailed examination of hydrides platelet at a step size of 0.1 μm. Texture and microstructure data were analyzed by the ATEX software [27].

3. Result

3.1 The orientation relationships of α-Ti / δ-hydride transition

Four types of orientation relationships have been reported in refs [17–20], which are shown in Table 1. In this work, just OR1 and OR2 were observed. The two most common orientation relationships (OR1 and OR2) of α-Ti/δ-hydride transition are similar to the hexagonal closed-packed (HCP)→face-centered cubic (FCC) phase transformation during plastic deformation in α-Ti [28]. Thus, these two ORs of α-Ti / δ-hydride transition can also be classified into basal-transformation (B-type transformation) and prismatic transformation (P-type transformation) like that in HCP / FCC phase transformation of titanium [28]. The widely observed B-type transformation adopts habit plane $\{0001\}_{\alpha}//\{1\bar{1}1\}_{\delta}$ $<1\bar{2}10>_{\alpha}//<110>_{\delta}$ and interface plane $\{10\bar{1}3\}_{\alpha}//\{1\bar{1}0\}_{\delta}$, accomplished via the gliding of Shockley partial dislocation on every two (0001) planes to change the stacking sequence from …ABABAB… to …ABCABC… [29]. Weatherly et al. [29] claimed that shearing caused by $1/3 <10\bar{1}0>$ Shockley partial dislocations to realize the change of stacking sequence AB→ABC associated with δ-hydride transition could not occur easily if driven only by mechanical stress, but it is feasible under the influence of a chemical stress driven by the high hydrogen concentration. The P-type transformation, with habit plane $\{0001\}_{\alpha}//\{001\}_{\delta}$ $<1\bar{2}10>_{\alpha}//<110>_{\delta}$ and interface plane $\{10\bar{1}0\}_{\alpha}//\{1\bar{1}0\}_{\delta}$, is considered to be formed via pure-shuffle mechanism on prismatic plane [30].

In order to identify different hydride platelets in EBSD maps, the two ORs (B-type and P-type) of hydrides are divided into different variants according to their interface planes (see Table 2). B-type and P-type hydride variants are notated as Bi and Pj, respectively (i=1,2,3…6 and j=1,2,3).

3.2 Orientation dependence of hydride layer

3.2.1 Microstructure characterization before and after hydrogen charging

In order to determine the microstructure of the initial α-Ti grains and the produced hydrides, EBSD maps were acquired on the diffusion surface of Sample A and Sample B (Surface A and Surface B) before and after hydrogen charging. Fig. 2a and 2c presents the microstructure of the initial material with equiaxed grains after heat treatment in form of inverse pole figure (IPF) map, where the X_3 axis (normal direction of the surface or diffusion direction of hydrogen) is projected with the shown color bar. The length direction and width direction are defined as X_1 and X_2, respectively. The average grain size of Sample A and Sample B is 29.4 and 25.5 μ m, respectively. The observation plane in Fig. 2 is the diffusion surface. The scattered points of the grains on the two surfaces are presented in the IPFs shown in Fig. 2a and 2c. The diffusion direction is close to <0001> of most grains on Surface A, while it is away from <0001> of the grains on Surface B. Thus, almost all kinds of orientations can be obtained from these two surfaces to investigate the orientation dependence of hydride precipitation.

After hydrogen charging, the microstructure is shown in Fig. 2b and 2d, in forms of phase map. In the phase maps, the blue color refers to the transformed FCC δ-hydride, while the red is the remnant HCP α-Ti phase. The grains (blue in phase map) are preferential for hydride formation, while the grains with large amount of red phase are difficult for hydriding. It should be noted that there are certain areas shown in white color, which are the non-indexed. The non-indexed areas are presumably due to the large lattice distortion inside the grains introduced by hydride precipitation. Indeed, large lattice misfit is caused due to the phase transformation from HCP α-Ti to FCC δ-hydride [17]. The non-indexed grains are difficult to accommodate the distortion of hydride transition and thus are not considered for hydride formation.

On Surface A in Fig. 2b, 57.33% of the total areas are identified as δ-hydride, 8.05% are α-Ti and the rest have zero solutions. As for the phase map of Surface B (Fig. 2d), significant increase of the red phase (HCP α-Ti, 57.02%) can be observed, while the proportions for the

blue phase (FCC δ-hydride, 24.03%) and zero solutions decrease. Thus, Surface A is easier to form hydride than Surface B. Although there are more preferential hydride nucleation sites (grain boundaries) in Sample B with slightly smaller grain size, the unfavorable texture significantly restrains the formation of hydride precipitation. Besides, the area fraction of the δ-hydride varies from one grain to another in phase maps, which indicates that the formation of hydride layer exhibits strong grain orientation dependence. This effect can be inferred from the comparison between the initial microstructure (Fig. 2a and 2c) and the hydrogen-charged microstructure (Fig. 2b and 2d), which will be discussed in details in the following sections.

To compare the texture change during hydriding on two surfaces, all the grain orientations are projected under the same coordinate, which is set up as X // TD, Y // RD and Z // ND. The grain orientations of Surface A and Surface B (rolled α-Ti sheet after heat treatment) before hydrogen charging are projected into {0001} pole figure (Fig. 2a and 2c). They exhibit similar split basal texture. After hydrogen charging, the {100} and {111} pole figures of δ-hydride (blue phase in phase map) are shown in Fig. 2b and 2d. The difference between the texture of hydride precipitation on Surface A and on Surface B suggests that the ORs of hydride transition on these two surface are different. Specially, at the same peak in {0001} pole figure of initial α-Ti, there are also two peaks in {001} pole figure of δ-hydride on Surface B, but no peaks in the {001} pole figure of surface A. It reveals that more hydrides follow P-type OR ($\{0001\}_\alpha$//$\{001\}_\delta$ $<1\bar{2}10>_\alpha$//$<110>_\delta$) with the initial matrix on Surface B than on Surface A. There are also two peaks in {111} pole figure of δ-hydride at the same location of {0001} pole figure of α-Ti. However, $\{0001\}_\alpha$//$\{111\}_\delta$ is followed by both B-type OR and OR4. Thus, the B-type OR was identified by comparing their pole figures of interface planes, which are different between these two ORs (see Table 1). These results are in agreement with that of zirconium reported in [12]. The P-type OR can be usually observed in the grains with c-axis away from the normal direction, which implies a higher resistant to hydride formation in these grains.

3.2.2 Classification of initial α-Ti grains

According to the different area fractions of hydride layer in grains after hydrogen charging (see in Fig. 2b and 2d), the initial grains of α-Ti can be divided into two groups as listed in Table 3. Group I represents the grains covered by hydride layer after hydriding (blue color in the phase maps). In this group, some grains with almost full blue in phase map means that they are fully covered by hydride layer, while some other grains with more than half blue phase are partially covered by hydride layer. According to the two ORs of hydride transition,

the as-received grains in Group I are further divided into B-type and P-type, which prefer to form B-type hydride layer and P-type hydride layer during hydriding, respectively. The grains with almost white (non-indexed) or red (remnant α-Ti matrix) in phase map are classified into Group II, which are difficult to form hydride layer during hydrogen charging. The number of the grains belonging to the two groups on Surface A and Surface B is shown in the Table 3.

Fig. 3a and 3d show the grains of Group I on Surface A and Surface B, respectively. By identifying the type of the orientation relationship between the initial α-Ti grain and the precipitated δ-hydride, the initial grains in Fig. 3a are further separated into B-type grains (Fig. 3c) and P-type grains (Fig. 3d). Excluding grains at the scanning border, 180 of the 186 grains in Fig. 3a are B-type grains in Fig. 3b and only 6 are P-type grains in Fig. 3c. On Surface B, just 7 in the total 62 of as-received α-Ti grains (Fig. 3d) which can form hydride layer are covered by B-type hydride (see Fig. 3e) and the other 55 grains (Fig. 3f) form P-type hydride layer. Therefore, B-type hydride is easier to be formed on Surface A during hydriding, while the formation of P-type hydride is more favorable on Surface B.

Comparing the two IPFs of α-Ti grains in Fig. 3a and 3d, more orientations on Surface A are favorable for hydride formation than Surface B, which attributes to the formation of more hydride on Surface A. Moreover, the IPFs are also divided into two areas, i.e., the B-type grains are located in the area inside red lines and the P-type grains are concentrated in the corner of the IPF (inside blue line). The area inside red lines on Surface A (Fig. 3a) is larger than that on Surface B (Fig. 3d), which indicates more B-type grain orientations on Surface A. Thus, more B-type hydrides are formed on Surface A. Similarly, more P-type grains formed on Surface B because more orientations on Surface B are favorable for P-type hydride transition as revealed in Fig. 3d. Interestingly, some B-type orientations on Surface A change into P-type on Surface B. It seems that the type of hydrides can be influenced by the preferentially formed hydrides in the neighboring grains.

3.2.3 Crystal orientation dependence of hydride precipitation

According to the microstructure of the hydride layer after hydrogen charging, four groups of initial grains were chosen from Surface A or B to explore the orientation dependence of hydride precipitation. EBSD maps and corresponding IPFs are shown in Fig. 4. Fully-covered B-type and P-type hydride layer form within the grains in Fig. 4a and 4b after hydriding, respectively. Fig. 4c and 4d present two kinds of grains, which are difficult to form hydride layer. One kind of grains in Fig. 4c is almost non-indexed after hydriding and the other in Fig. 4d is nearly full of remnant α-Ti matrix.

9

Fig. 4a shows that the orientations most favorable for B-type transition are focused in the position where the X_3 axis deviates 30° from $<0001>$ direction to $<10\bar{1}0>$ direction, which implies that $\{10\bar{1}3\}$ plane is parallel to the diffusion surface. However, the grains in Fig. 4c exhibit the most favorable orientations for P-type transition with $\{10\bar{1}0\}$ plane parallel to surface. As shown in Fig. 4b and 4d, the most unfavorable orientations for the formation of hydride are in the position where c-axis and a-axis are normal to the diffusion surface, respectively.

According to the phase maps in Fig. 2 together with Fig. 4, more non-indexed grains (white color) exist on Surface A after hydriding than on Surface B. It results from more initial grains on Surface A with the orientation of c-axis parallel to the diffusion direction. More grains with a-axis parallel to the diffusion direction on Surface B result in more remnant α-Ti matrix (red color) after hydriding (Fig. 2d). The reason will be further discussed in section 4.3.2.

3.3 Characterization of hydride platelets

During hydriding, the hydride platelets (Fig. 5) were formed inside the matrix at first, before the formation of covered thin hydride layer. Further understanding of the hydride nucleation process can be provided through the characterization of hydride platelets, which was conducted by removing the thin hydride layer from sample surface via electrolytic polishing.

The hydride platelets are imbedded in the α-Ti matrix, as shown in Fig. 5. The contrast of the FSD map (Fig. 5) based on diffraction events at each pixel indicates the deformation and strain gradient in the material. The different contrasts show the various degrees of lattice deformation upon the formed hydrides. The dark platelets contain large lattice deformation, while the hydrides with little distortion are light. Similar to the hydride layer, the microstructure of hydride platelets also varies form one grain to another. Three types of microstructures (inside red circles) are observed within the field-of-view: Type I (parallel hydride platelets), Type II (crossed hydride platelets) and Type III (clustered hydride platelets). The multiple morphologies of hydride platelets suggest that the hydride process involves variant selection of hydride precipitation and interaction of different variants. To characterize different microstructures of hydride platelets, detailed EBSD measurement was performed, which will be presented in section 4.3.

4. Discussion

4.1 Orientation relationship preference of α-Ti / δ-hydride transition

In order to understand the phase transition process, it is a significant issue to study the ORs followed by δ-hydride with α-Ti matrix. Two types of ORs associated with α-Ti / δ-hydride transition were observed in the present work: B-type and P-type. The anisotropic misfit strain induced by α-Ti / δ-hydride phase transformation will be calculated to explain the OR preference.

The total volume strain of phase transition from α-Ti (a_α = 0.295 nm, c_α = 0.468 nm) to δ-hydride (a_δ = 0.440 nm) is calculated. The volume per atom (V) is defined as the volume of a lattice cell of the crystal divided by the nominal atom number of the lattice cell (6 atoms for HCP Ti and 4 for FCC hydride), i.e., $\sqrt{3}\, a_\alpha^2 c_\alpha/4$ for α-Ti and $a_\delta^3/4$ for δ-hydride. The calculated results for α-Ti (V_α) and δ-hydrides (V_δ) are $1.76{\times}10^{-29}$ m^3 and $2.13{\times}10^{-29}$ m^3, respectively. The volume strain during α-Ti / δ-hydride transformation is constant for different ORs and can be obtained by: $(V_\alpha - V_\delta)/V_\alpha$, equal to 20.6%.

For each OR, the misfit parameters of the α-Ti / δ-hydride transition were further examined by the calculation method proposed in [31]. For B-type transition, i.e., $\{0001\}_\alpha//\{1\bar{1}1\}_\delta$ $<1\bar{2}10>_\alpha//<110>_\delta$, the atomic spacing on the basal plane along the $<1\bar{2}10>$ and $<10\bar{1}0>$ direction expand from 0.295 nm to 0.311 nm and from 0.511 nm to 0.539 nm, respectively. The atomic spacing perpendicular to the basal plane expands along $<0001>$ from 0.234 nm to 0.254 nm. These atomic spacing expansions in each direction corresponds to lattice strains of 5.5%, 5.5% and 8.6%, respectively. Similarly, for P-type transition, i.e., $\{0001\}_\alpha//\{001\}_\delta$ $<1\bar{2}10>_\alpha//<110>_\delta$, atomic spacing reduced by -6.0% from 0.234 nm to 0.220 nm along $<0001>$, while increased by 5.5% along $<1\bar{2}10>$ and by 21.8% along $<10\bar{1}0>$ on the basal plane. Comparing the misfit parameters between these two types of ORs, the largest strain along $<10\bar{1}0>$ of P-type transition (21.8%) produces larger distortion on the basal plane. Therefore, P-type OR for hydride transition in α-Ti is less favorable than B-type.

In addition, the other two ORs (OR3 $\{10\bar{1}1\}_\alpha//\{1\bar{1}1\}_\delta$ $<1\bar{2}10>_\alpha//<110>_\delta$ and OR4 $\{\bar{1}011\}_\alpha//\{001\}_\delta$ $<1\bar{2}10>_\alpha//<110>_\delta$) are unfavorable and are not observed in our experiment. For OR3, the expansion strain along $<0001>$ is 15.0%. Such a large strain along c-axis is difficult to be accommodated by dislocations in titanium. Another possible reason is that the average density of coinciding atoms in the $\{0001\}_\alpha//\{1\bar{1}2\}_\delta$ interface plane of OR3 is the lowest among these four ORs [17]. The OR4 and B-type OR are quite close except different

11

interface planes, which is $\{10\bar{1}1\}$ for OR4 and $\{10\bar{1}3\}$ for B-type. $\{10\bar{1}3\}$ is a favorable interface plane for strain release during hydride transition (see the details in section 4.2). Therefore, B-type and P-type OR are the major orientation relationships drawn in this work.

4.2 Strain anisotropy of α-Ti / δ-hydride phase transformation

The δ-hydride phase transformation is multi-step process in zirconium and the shape evolution of the δ-hydride is highly dependent on the intermediate ζ and γ phase [32]. Different from zirconium, only one type of intermediate phase (γ phase) has been observed in titanium so far. In this section, anisotropic strain in α-Ti matrix caused by the two-step phase transformation is calculated based on the transformation of deformation gradient tensors to explore the origins of orientation dependence for the hydride formation.

The deformation gradient tensors of Variant 1 obeying B-type and P-type hydride transition are shown in Table 4, expressed in the crystal coordination frame (see Fig. 6) with x_1, x_2 and x_3 axis along the $[10\bar{1}0]$, $[\bar{1}2\bar{1}0]$ and $[0001]$ of α-Ti matrix, respectively. The details of the calculation of the deformation gradient tensors are shown in Appendix A. In the tensors, the diagonal elements, D_{ij} ($i=j$, i, $j=1$, 2 3), mean elongation ($D_{ii} > 1$) or contraction ($D_{ii} < 1$), whereas, the off diagonal elements, (D_{ij}, $i{\neq}j$) indicate shear in the direction of i on the plane normal to j. For the tensor of B-type transition in Table 4, $D_{11} = D_{22}$, it shows the isotropic misfit on the basal plane, while the misfit along c-axis (x_3 axis), D_{33}, is higher than that in x_1-x_2 plane. A large shear occurs on the basal plane, D_{13}, which changes the orientation and stacking structure of the δ-hydride. In addition, the misfit of P-type transition along x_1 axis (D_{11}) is much higher than the other, which results in large distortion on the basal plane. These displacement tensors indicate a possible platelet-like shape of δ-hydride precipitation and anisotropic growth to minimize the deformation energy.

The anisotropic misfit strain of α-Ti / δ-hydride transition was calculated along different crystal directions (details of calculation are shown in Appendix A). The results are projected into the full inverse pole figure with the shown color bar (see Fig. 7). The orange area shows the crystal directions with the largest misfit strain. The grains with these crystal directions normal to diffusion surface can relax the largest expansion misfit of hydride transition through the free surface. Thus, they are the most favorable ones for the hydride formation. Conversely, the most unfavorable grains are those with crystal directions in white area normal to diffusion surface.

The strain IPF for Variant 1 of B-type transition is shown in Fig. 7a. The high strain area (orange) is nearly an ellipse with the maxima of 28.0% along the $\{10\bar{1}2.6\}$ plane normal, which is 3.76° deviated from the most favorable orientation, i.e., $\{10\bar{1}3\}$ interface plane normal. In fact, the energy of phase transformation can be adjusted by anisotropy interfacial energy through reducing the tilt angle of the hydride interface plane towards basal plane [14]. Fig. 7b is a full strain IPF projected by the maximum strain of all six B-type hydride variants during the transition. The strain map is six-fold symmetric around c-axis. It shows that the grain orientations with $\{10\bar{1}3\}$ plane parallel to the sample surface are the most preferential and those with basal plane normal to the surface are the most unfavorable for B-type hydride transformation.

For P-type transition, the peak area (orange) of the strain IPF for Variant 1 in Fig. 7c is around $\{10\bar{1}0\}$ plane normal with the maxima of 21.8%. It can be seen in Fig. 7d with all the six variants of P-type hydride that the six high peak areas are around $\{10\bar{1}0\}$ plane normal, while the area with minimal strain value is located around c-axis. Thus, for P-type hydride transformation, the orientations with $\{10\bar{1}0\}$ and $\{0001\}$ plane parallel to the sample surface are the most preferential and unfavorable orientation, respectively. This conclusion for P-type transition is in good agreement with the experimental result. The influence of anisotropic interfacial energy is negligible due to the large distortion on the basal plane.

4.3 Classified characterization of hydride platelets

To research the relationship between hydride nucleation and crystal orientation, EBSD measurements were performed on five typical grains. As presented in Fig. 8, five areas are labeled in the inverse pole figure (Areas 1-5). In Area 1 and Area 2, the grains are fully covered by hydride layer after hydriding. In Area 3, partially covered hydride layer is generated in the grains. All the grains with orientations in Areas 1-3 belong to Group I. In addition, Areas 4-5 represent the orientations of grains belonging to Group II. After hydriding, the grains in Area 4 are almost non-indexed and those in Area 5 are full of remnant α-Ti matrix. The morphologies of hydride platelets were acquired in five representative grains (Grains 1-5) with the orientations chosen from Areas 1-5, respectively (see Fig. 9 and Fig. 10).

4.3.1 Grains with one or two preferential hydride variants (Group I)

Grain 1 in Fig. 9a first form several parallel hydride platelets before fully covered by B-type hydride layer. These platelets grow and merge with each other. As a result, they cover the whole grain quickly and then hinder subsequent diffusion of hydrogen. In the

$\{10\bar{1}3\}//\{1\bar{1}0\}$ pole figure (Fig. 9a), B5 is the only hydride variant and the $\{1\bar{1}0\}$ pole of the selected variant is the closest to the center of the pole figure. According to section 4.2, the hydride variants with interface plane parallel to the diffusion surface is the most preferred due to the highest capacity of strain release. Thus, hydride variant selection can be evaluated by calculating the distance (d) between the interface plane pole of different variants and the center of pole figure. The hydride variants with smaller d, which means that larger distortion can be accommodated through free surface, are easier to be formed. It should be noted that the value of d cannot be used for the variant selection associated with different types of hydride transition. For Grain 1, the value d of possible six B-type variants is shown in the Table 5. Among all the variants of B-type transition, B5 has the minimum d of 0.169 and thus it is the most favorable B-type variant. In conclusion, the grains with such orientation only favor one hydride variant. The $\{10\bar{1}3\}//\{1\bar{1}0\}$ interface plane of the selected variant is nearly parallel to the diffusion surface. Besides, Fig. 9a also shows that the hydrides near grain boundaries can stimulate the hydride nucleation in neighbouring grains. The growth of both intragranular hydrides and hydrides across grain boundaries is achieved via an auto-catalytic mechanism [16].

Fig. 9b presents Grain 2 with the orientation favorable for P-type hydride, i.e., $\{10\bar{1}0\}$ plane nearly parallel to the sample surface. Due to the large distortion on basal plane of P-type transition, the formation of hydride layer is more difficult and the thickness is extremely thin. Therefore, after electrolytic polishing, only a few parallel platelets of P-type hydrides are left in Grain 2 and they are always accompanied by some B-type hydrides and micro twins (see Fig. 9b). From the pole figures in Fig. 9b, the hydride variants are P2 and B5. The $\{1\bar{1}0\}$ pole of P2 is much closer to the center of pole figure than the $\{1\bar{1}0\}$ pole of B5. Besides, the value d of P2 and B5 in Table 5 is the smallest among the variants of P-type and B-type, respectively. Thus, P2 is the most preferential hydride variant in Grain 2. It seems that B5 is stimulated by the B-type hydride in the neighbouring grain (pink), which is favorable for B-type transition like Grain 1.

For Grain 3, it is partially covered by hydride layer after hydriding. The hydrides inside with crossed-lamellar microstructure is shown in Fig. 9c. Two B-type variants precipitate and intersect with each other. These two variants are $\{111\}$ $<11\bar{2}>$ twins (similar to the observation in zirconium reported by Wang et al. [16]). The stress concentration caused by the boundaries between the two variants restrains their further growth. Thus, only partial grain is covered by hydride layer after hydriding. The pole figure in Fig. 9c shows that the two

14

variants are B2 and B3. The $\{1\bar{1}0\}$ poles of them align most closely to the center of the pole figure and they have similar values (d) shown in Table 5. If two B-type variants are selected simultaneously in one grain, they are definitely adjacent variants, i.e., Bi and Bi+1. However, two or three P-type variants formed in the same grain can only occur when they are in pairs with B-type variants, which will be presented in Fig. 10b.

4.3.2 Grains with more than three hydride variants (Group II)

Grain 4, with ***c***-axis normal to the sample surface, are almost non-indexed after hydriding. Fig. 10a shows the morphology of the microstructure after removing the non-indexed hydride layer via electropolishing. The fine platelets in Grain 4 are intercrossed. Some $\{10\bar{1}2\}$ $<\bar{1}011>$ extension twins are induced at the $\{10\bar{1}3\}$ interface of hydride platelets. According to the pole figures in Fig. 10a, all the six B-type variants are formed in this grain. It is because that the $\{10\bar{1}3\}$ poles of α-Ti matrix are nearly six-fold symmetric around surface normal and the distance values (d) of them are similar (see Table 6). According to the misorientation between them, the six B-type hydride variants can be divided into two groups: Bi $\rightarrow$ Bi+1, Bi+3 and Bi+5 (twin 60° / $<11\bar{1}>$); Bi $\rightarrow$ Bi+2 and Bi+4 (no obvious misorientation). Furthermore, the deformation of these six variants along different directions produces large distortion in Grain 4. Thus, the reason why the grains with the orientations like Grain 4 are always non-indexed after hydrogen charging is the large distortion produced by the interaction between the multiple variants.

The ***a***-axis of Grain 5 is nearly parallel to the surface normal. After hydriding, the grains with this kind of orientation usually remain large amount of α-Ti matrix. The clustered hydride platelets are observed in Fig. 10b after electropolishing. From the pole figures in Fig. 10b, the clusters include both B-type and P-type hydride platelets. The B-type hydride variants are B4 and B5, and the P-type variants are P1 and P2. Occasionally, B3 can be stimulated near the junction of B4 and B5. According to the misorientation, three P-type variants are classified into two groups: Pi $\rightarrow$ Pi+1 (30° / $<0001>$); Pi $\rightarrow$ Pi+2 (no obvious misorientation). Besides, Pi $\rightarrow$ Bi and Bi+3 are often observed in pairs, with the misorientation of 60° around $<11\bar{2}0>$, i.e., ***a***-axis of the surrounding titanium matrix. It is therefore speculated that the Pi is stimulated by Bi or Bi+3 through dislocation reaction on the basal plane of the Ti matrix.

The formation of B-type hydride is difficult in Grain 5 because the minimum value d (Table 6) is larger than that in Grain 1 and Grain 3 (Table 5). The finer P-type hydride

platelets show that P-type hydride is more difficult to nucleate in Grain 5. Besides, the interaction of different B-type and P-type hydride variants in each cluster restrains the growth of hydride clusters. They finally result in large amount of remnant α-Ti matrix in the grain with the orientation like Grain 5 after hydriding.

5. Conclusion

Two typical orientation relationships of α-titanium / δ-hydride transition (B-type: $\{0001\}_\alpha//\{1\bar{1}1\}_\delta$ $<1\bar{2}10>_\alpha//<110>_\delta$ with interface plane $\{10\bar{1}3\}_\alpha//\{1\bar{1}0\}_\delta$, and P-type: $\{0001\}_\alpha//\{001\}_\delta$ $<1\bar{2}10>_\alpha//<110>_\delta$ with interface plane $\{10\bar{1}0\}_\alpha//\{1\bar{1}0\}_\delta$) are revealed by using interrupted in-situ microstructure characterization on diffusion surfaces before and after electrolytic hydrogen charging. The grain orientations with $\{10\bar{1}3\}$ and $\{10\bar{1}0\}$ interface planes parallel to the diffusion surface are most favorable for B-type and P-type hydride transition, respectively. However, *c*-axis and *a*-axis of α-Ti grains parallel to the diffusion direction are the most unfavorable orientations for the formation of hydride precipitation. The calculation of anisotropic strain caused by hydride transition in α-Ti matrix indicates that the grains which are more favorable for hydride formation can more effectively accommodate the strain of hydride transition through the diffusion surface. In addition, three types of hydride platelet microstructures are observed: parallel hydride platelets (Type I), crossed hydride platelets (Type II) and clustered hydride platelets (Type III). The multiple morphologies of hydride platelets associated with the interaction between different hydride variants are found to be dependent on the grain orientation.

Acknowledgements

Appendix A

We calculate the strain of B-type hydride transition using the method of Woo [21].The phase transformation (HCP titanium-FCT hydride-FCC hydride) can be achieved by the passage of $1/3\langle 10\bar{1}0\rangle$ partial dislocations on the basal plane that are associated with lattice transformation. The coordinate systems selected in the current work is shown as follows:

x_1 : $[10\bar{1}0]_\alpha \rightarrow [\bar{1}12]_\delta \Rightarrow \sqrt{3}a_\alpha \rightarrow \sqrt{6}a_\delta/2$

x_2 : $[\bar{1}2\bar{1}0]_\alpha \rightarrow [110]_\delta \Rightarrow a_\alpha \rightarrow \sqrt{2}a_\delta/2$

x_3 : $[0001]_\alpha \rightarrow [1\bar{1}1]_\delta \Rightarrow c_\alpha \rightarrow 2d_{(1\bar{1}1)_\delta} = 2a_\delta/\sqrt{3}$

The first step in the calculation is to dilate the c/a ratio for Ti from 1.588 to 1.633 (the ideal value for HCP), followed by a simple shear of Shockley dislocation. This converts the Ti lattice to a FCC structure with a lattice parameter $a = 0.417$ nm.

The lattice transformation matrix $\mathbf{M_1}$ from α-Ti lattice to ideal HCP lattice can be written as follows:

$$\mathbf{M_1} = \begin{bmatrix} 1 & 0 & 0 \\ 0 & 1 & 0 \\ 0 & 0 & m \end{bmatrix} \tag{1}$$

with $m = 1.633/1.588 = 1.028$

To realize HCP/FCC transition, shearing along $[10\bar{1}0]$ is necessary to change of stacking sequence AB/ABC, leading to δ-phase generation. By physical or crystallographic studies, we know the shear plane normal $\boldsymbol{p_0}$ and the shear vector $\boldsymbol{d} = n\boldsymbol{d_0}$ ($n = \sqrt{2}/4$), $\boldsymbol{p_0}$ and $\boldsymbol{d_0}$ are taken as unit vectors, then the pure shear matrix can be written directly:

$$\mathbf{S} = (\mathbf{I} + n\,\boldsymbol{d_0}\,\boldsymbol{p_0^T}) \tag{2}$$

The deformation gradient matrix $\mathbf{S}$ arising from this shearing can be written as:

$$\mathbf{S} = (\mathbf{I} + n[100]_\alpha[001]_\alpha) = \begin{bmatrix} 1 & 0 & 0 \\ 0 & 1 & 0 \\ 0 & 0 & 1 \end{bmatrix} + n\begin{bmatrix} 0 & 0 & 1 \\ 0 & 0 & 0 \\ 0 & 0 & 0 \end{bmatrix} \tag{3}$$

Therefore, the total transformation matrix, that is deformation gradient tensor, becomes:

$$\mathbf{T} = \mathbf{M_1}\mathbf{S} \tag{4}$$

There are six variants:

$\boldsymbol{d_0}$	$\boldsymbol{p_0}$	$\mathbf{S}_i$	$\mathbf{T}_i = \mathbf{M_1}\mathbf{S}_i$
$[10\bar{1}0]$	$[0001]$	$\mathbf{S_1} = \begin{bmatrix} 1 & 0 & 2n_1 \\ 0 & 1 & 0 \\ 0 & 0 & 1 \end{bmatrix}$	$\mathbf{T_1} = \begin{bmatrix} 1 & 0 & 2n_1 \\ 0 & 1 & 0 \\ 0 & 0 & m \end{bmatrix}$
$[01\bar{1}0]$	$[0001]$	$\mathbf{S_2} = \begin{bmatrix} 1 & 0 & n_1 \\ 0 & 1 & n_2 \\ 0 & 0 & 1 \end{bmatrix}$	$\mathbf{T_2} = \begin{bmatrix} 1 & 0 & n_1 \\ 0 & 1 & n_2 \\ 0 & 0 & m \end{bmatrix}$
$[\bar{1}100]$	$[0001]$	$\mathbf{S_3} = \begin{bmatrix} 1 & 0 & -n_1 \\ 0 & 1 & n_2 \\ 0 & 0 & 1 \end{bmatrix}$	$\mathbf{T_3} = \begin{bmatrix} 1 & 0 & -n_1 \\ 0 & 1 & n_2 \\ 0 & 0 & m \end{bmatrix}$
$[\bar{1}010]$	$[0001]$	$\mathbf{S_4} = \begin{bmatrix} 1 & 0 & -2n_1 \\ 0 & 1 & 0 \\ 0 & 0 & 1 \end{bmatrix}$	$\mathbf{T_4} = \begin{bmatrix} 1 & 0 & -2n_1 \\ 0 & 1 & 0 \\ 0 & 0 & m \end{bmatrix}$
$[0\bar{1}10]$	$[0001]$	$\mathbf{S_5} = \begin{bmatrix} 1 & 0 & -n_1 \\ 0 & 1 & -n_2 \\ 0 & 0 & 1 \end{bmatrix}$	$\mathbf{T_5} = \begin{bmatrix} 1 & 0 & -n_1 \\ 0 & 1 & -n_2 \\ 0 & 0 & m \end{bmatrix}$
$[1\bar{1}00]$	$[0001]$	$\mathbf{S_6} = \begin{bmatrix} 1 & 0 & n_1 \\ 0 & 1 & -n_2 \\ 0 & 0 & 1 \end{bmatrix}$	$\mathbf{T_6} = \begin{bmatrix} 1 & 0 & n_1 \\ 0 & 1 & -n_2 \\ 0 & 0 & m \end{bmatrix}$

with $n_1 = n/2$ and $n_2 = \sqrt{3}n/2$

The FCC structure is further dilated to the γ-structure, $a = 0.420$ nm, $c = 0.470$ nm, in the second step. The lattice transformation matrix $\mathbf{B_2}$ from FCC lattice to FCT hydride lattice, referred to the Ti axes is:

$$\mathbf{B_1} = \mathbf{A^{-1}}\mathbf{M_2}\mathbf{A} \tag{5}$$

where $\mathbf{A} = \begin{bmatrix} -1/\sqrt{6} & 1/\sqrt{2} & 1/\sqrt{3} \\ 1/\sqrt{6} & 1/\sqrt{2} & -1/\sqrt{3} \\ 2/\sqrt{6} & 0 & 1/\sqrt{3} \end{bmatrix}$ and $\mathbf{M_2} = \begin{bmatrix} r_1 & 0 & 0 \\ 0 & r_1 & 0 \\ 0 & 0 & s_1 \end{bmatrix}$, with $r_1 = 0.420/0.417$, $s_1 = 0.470/0.417$.

For the third step, the lattice transformation matrix $\mathbf{B_2}$ from metastable γ-structure to FCC δ-hydride ($a = 0.440$ nm) is:

$$\mathbf{B_2} = \mathbf{A^{-1}}\mathbf{M_3}\mathbf{A} \tag{6}$$

where $\mathbf{M_3} = \begin{bmatrix} r_2 & 0 & 0 \\ 0 & r_2 & 0 \\ 0 & 0 & s_2 \end{bmatrix}$, with $r_2 = 0.440/0.420$, $s_2 = 0.440/0.470$.

Combining these three steps, the deformation gradient tensor of B-type α-Ti/δ-hydride transformation is:

$$\mathbf{D_B} = \mathbf{B_2}\mathbf{B_1}\mathbf{T} \tag{7}$$

If we assume that a given vector $\boldsymbol{u}$ in the coordinates of the α phase is transformed to $\boldsymbol{v}$ due to the transformation, the transformation strain ε along each orientation can be calculated as follows:

$$\varepsilon_B = (|\boldsymbol{v}| - |\boldsymbol{u}|)/|\boldsymbol{u}| \tag{8}$$

where $\boldsymbol{v} = \mathbf{D_B}\boldsymbol{u}$

17

For the strain calculation of P-type hydride formed by pure-shuffle mechanism [30], we just consider the lattice transformation without shearing. The coordinate systems selected in the current work is shown as follows:

$x_1 : [10\bar{1}0]_\alpha \rightarrow [1\bar{1}0]_\delta \Rightarrow \sqrt{3}a_\alpha \rightarrow \sqrt{2}\,a_\delta$

$x_2 : [\bar{1}2\bar{1}0]_\alpha \rightarrow [110]_\delta \Rightarrow a_\alpha \rightarrow \sqrt{2}a_\delta/2$

$x_3 : [0001]_\alpha \rightarrow [001]_\delta \Rightarrow c_\alpha \rightarrow a_\delta$

The first step in the calculation of P-type hydride transformation is to dilate HCP α-Ti (a = 0.295 nm, c = 0.468 nm) to FCT γ-hydride. The lattice transformation matrix is:

$$\mathbf{P_1} = \begin{bmatrix} \xi_1 & 0 & 0 \\ 0 & \xi_2 & 0 \\ 0 & 0 & \xi_3 \end{bmatrix} \tag{9}$$

with $\xi_1 = \frac{\sqrt{6}}{3}\frac{a_\gamma}{a_\alpha}$; $\xi_2 = \frac{\sqrt{2}}{2}\frac{a_\gamma}{a_\alpha}$; $\xi_3 = \frac{c_\gamma}{c_\alpha}$;

The lattice transformation matrix from γ-hydride to δ-hydride in the second step is:

$$\mathbf{P_2} = \begin{bmatrix} \xi_1 & 0 & 0 \\ 0 & \xi_2 & 0 \\ 0 & 0 & \xi_3 \end{bmatrix} \tag{10}$$

with $\xi_1 = \frac{\sqrt{6}}{3}\frac{a_\delta}{a_\gamma}$; $\xi_2 = \frac{\sqrt{2}}{2}\frac{a_\delta}{a_\gamma}$; $\xi_3 = \frac{a_\delta}{c_\gamma}$;

Thus, the deformation gradient tensor of P-type α-Ti/δ-hydride transformation can be written as follows:

$$\mathbf{D_P} = \mathbf{P_2}\mathbf{P_1} \tag{11}$$

The transformation strain ε along each orientation can be calculated as follows:

$$\varepsilon_P = (|\mathbf{v}|-|\mathbf{r}|)/|\mathbf{r}| \tag{12}$$

where $\mathbf{v} = \mathbf{D_P}\mathbf{r}$

References

[1]   D. Banerjee, J.C. Williams, Perspectives on titanium science and technology, Acta Mater. 61 (2013) 844–879. doi:10.1016/j.actamat.2012.10.043.

[2]   D.G. Ivey, D.O. Northwood, Storing energy in metal hydrides: a review of the physical metallurgy, J. Mater. Sci. 18 (1983) 321–347. doi:10.1007/BF00560621.

[3]   D.S. Shih, I.M. Robertson, H.K. Birnbaum, Hydrogen embrittlement of alpha titanium : in situ TEM studies, Acta Metall. 36 (1988) 111–124. doi:10.1016/0001-6160(88)90032-6.

[4]   H.K. Birnbaum, Mechanical properties of metal hydrides, J. Less-Common Met. 104 (1984) 31–41. doi:10.1016/0022-5088(84)90433-8.

[5]   I.M. Robertson, T. Tabata, W. Wei, F. Heubaum, H.K. Birnbaum, Hydrogen embrittlement and grain boundary fracture, Scr. Metall. 18 (1984) 841–846. doi:10.1016/0036-9748(84)90407-1.

[6]   J.G. Morlet, H.H. Johnson, A.R. Troiano, C.I. of Technology, A new concept of hydrogen embrittlement in steel, Wright Air Development Center, Air Research and Development Command, United States Air Force, 1957.

[7]   A.R. Troiano, The role of hydrogen and other interstitials in the mechanical behavior of metals, Metallogr. Microstruct. Anal. 5 (2016) 557–569. doi:10.1007/s13632-016-0319-4.

[8]   G.J.C. Carpenter, J.F. Watters, R.W. Gilbert, Dislocations generated by zirconium hydride precipitates in zirconium and some of its alloys, J. Nucl. Mater. 48 (1973) 267–276. doi:10.1016/0022-3115(73)90023-8.

[9]   C.Q. Chen, S.X. Li, K. Lu, The deformation behaviors of gamma hydrides in titanium under cyclic straining, Acta Mater. 51 (2003) 931–942. doi:10.1016/S1359-6454(02)00495-0.

[10]   C.Q. Chen, S.X. Li, H. Zheng, L.B. Wang, K. Lu, An investigation on structure, deformation and fracture of hydrides in titanium with a large range of hydrogen contents, Acta Mater. 52 (2004) 3697–3706. doi:10.1016/j.actamat.2004.04.024.

[11]   S. Liu, Z. Zhang, S. Xiao, Y. Chen, Effect of hydrogenation on microstructure evolution, mechanical and electrochemical properties of pure titanium, J. Alloys Compd. 781 (2019) 1139–1149. doi:10.1016/j.jallcom.2018.11.038.

[12]   F. Long, D. Kerr, G. Domizzi, Q. Wang, M.R. Daymond, Microstructure characterization of a hydride blister in Zircaloy-4 by EBSD and TEM, Acta Mater. 129 (2017) 450–461. doi:10.1016/j.actamat.2017.03.016.

[13]   R.K. Sharma, S. Sunil, B.K. Kumawat, R.N. Singh, A. Tewari, B.P. Kashyap, Influence of hydride orientation on fracture toughness of CWSR Zr-2.5%Nb pressure tube material between RT and 300 °C, J.

Nucl. Mater. 488 (2017) 231–244. doi:10.1016/j.jnucmat.2017.03.025.

[14] G.M. Han, Y.F. Zhao, C.B. Zhou, D.Y. Lin, X.Y. Zhu, J. Zhang, S.Y. Hu, H.F. Song, Phase-field modeling of stacking structure formation and transition of δ-hydride precipitates in zirconium, Acta Mater. 165 (2019) 528–546. doi:10.1016/j.actamat.2018.12.009.

[15] W. Qin, N.A.P. Kiran Kumar, J.A. Szpunar, J. Kozinski, Intergranular δ-hydride nucleation and orientation in zirconium alloys, Acta Mater. 59 (2011) 7010–7021. doi:10.1016/j.actamat.2011.07.054.

[16] S. Wang, F. Giuliani, T. Ben Britton, Microstructure and formation mechanisms of δ-hydrides in variable grain size Zircaloy-4 studied by electron backscatter diffraction, Acta Mater. 169 (2019) 76–87. doi:10.1016/j.actamat.2019.02.042.

[17] E. Conforto, D. Caillard, A fast method for determining favourable orientation relationships and interface planes: Application to titanium-titanium hydrides transformations, Acta Mater. 55 (2007) 785–798. doi:10.1016/j.actamat.2006.06.061.

[18] A. Bourret, A. Lasalmonie, S. Naka, In-situ high resolution observation of hydride precipitation in titanium, Scr. Metall. 20 (1986) 861–866. doi:10.1016/0036-9748(86)90455-2.

[19] H. Numakura, M. Koiwa, Hydride precipitation in titanium, Acta Metall. 32 (1984) 1799–1807. doi:10.1016/0001-6160(84)90236-0.

[20] E. Conforto, D. Caillard, Edge-to-edge matching at Ti-TiH interfaces: kinetics of hydride growth and clustering of precipitates with different orientation relationships, Solid State Phenom. 172–174 (2011) 242–247. doi:10.4028/www.scientific.net/ssp.172-174.242.

[21] O.T. Woo, G.C. Weatherly, C.E. Coleman, R.W. Gilbert, The precipitation of γ-deuterides (hydrides) in titanium, Acta Metall. 33 (1985) 1897–1906. doi:10.1016/0001-6160(85)90011-2.

[22] N.A.P. Kiran Kumar, J.A. Szpunar, Z. He, Preferential precipitation of hydrides in textured zircaloy-4 sheets, J. Nucl. Mater. 403 (2010) 101–107. doi:10.1016/j.jnucmat.2010.06.005.

[23] N.A.P. Kiran Kumar, J.A. Szpunar, EBSD studies on microstructure and crystallographic orientation of δ-hydrides in Zircaloy-4, Zr-1% Nb and Zr-2.5% Nb, Mater. Sci. Eng. A. 528 (2011) 6366–6374. doi:10.1016/j.msea.2011.05.022.

[24] J. Wen, N. Main, E. Fleury, The effect of hydrogen-deformation interactions on recrystallization of β-21S titanium alloys, Proc. 13th World Conf. Titan. (2016) 275–280. doi:10.1002/9781119296126.ch41.

[25] J. Wen, N. Allain, E. Fleury, Hydrogen evolution and its effects on cold rolling behavior in commercial pure titanium, Mater. Charact. 121 (2016) 139–148. doi:10.1016/j.matchar.2016.10.002.

[26] Y.Z. Chen, H.P. Barth, M. Deutges, C. Borchers, F. Liu, R. Kirchheim, Increase in dislocation density in cold-deformed Pd using H as a temporary alloying addition, Scr. Mater. 68 (2013) 743–746. doi:10.1016/j.scriptamat.2013.01.005.

[27] B. Beausir and J.-J. Fundenberger, Analysis tools for electron and X-ray diffraction, ATEX - software, www.atex-software.eu, Université de Lorraine - Metz, 2017.

[28] X. Zheng, M. Gong, T. Xiong, H. Ge, L. Yang, Y. Zhou, S. Zheng, X. Ma, J. Wang, Deformation induced FCC lamellae and their interaction in commercial pure Ti, Scr. Mater. 162 (2018) 326–330. doi:10.1016/j.scriptamat.2018.11.037.

[29] G.C. Weatherly, The precipitation of γ-hydride plates in zirconium, Acta Metall. 29 (1981) 501–512. doi:10.1016/0001-6160(81)90074-2.

[30] C.N. Tomé, X.F. Bi, Z. Zhang, J. Wang, A. Kumar, H.C. Wu, S.X. Mao, Rolling-induced Face Centered Cubic Titanium in Hexagonal Close Packed Titanium at Room Temperature, Sci. Rep. 6 (2016) 1–8. doi:10.1038/srep24370.

[31] G.J.C. Carpenter, The dilatational misfit of zirconium hydrides precipitated in zirconium, J. Nucl. Mater. 48 (1973) 264–266. doi:10.1016/0022-3115(73)90022-6.

[32] J. Bair, M. Asle Zaeem, D. Schwen, Formation path of δ hydrides in zirconium by multiphase field modeling, Acta Mater. 123 (2017) 235–244. doi:https://doi.org/10.1016/j.actamat.2016.10.056.

Table 1 Four orientation relationships of α-Ti / δ-hydride transition

	Orientation relationship	Interface plane
OR1	$\{0001\}_\alpha//\{1\bar{1}1\}_\delta$ (angle of 4°), $<1\bar{2}10>_\alpha//<110>_\delta$	$\{10\bar{1}3\}_\alpha//\{1\bar{1}0\}_\delta$
OR2	$\{0001\}_\alpha // \{001\}_\delta$, $<1\bar{2}10>_\alpha//<110>_\delta$	$\{10\bar{1}0\}_\alpha//\{1\bar{1}0\}_\delta$
OR3	$\{10\bar{1}1\}_\alpha//\{1\bar{1}1\}_\delta$, $<1\bar{2}10>_\alpha//<110>_\delta$	$\{0001\}_\alpha//\{1\bar{1}2\}_\delta$
OR4	$\{\bar{1}011\}_\alpha//\{001\}_\delta$, $<1\bar{2}10>_\alpha//<110>_\delta$	$\{10\bar{1}1\}_\alpha//\{1\bar{1}\bar{1}\}_\delta$

Table 2 Hydride variants of B-type and P-type transitions

Hydride	Variant 1	Variant 2	Variant 3	Variant 4	Variant 5	Variant 6
B-type	$(10\bar{1}3)_\alpha$ $// (1\bar{1}0)_\delta$	$(01\bar{1}3)_\alpha$ $// (1\bar{1}0)_\delta$	$(\bar{1}103)_\alpha$ $// (1\bar{1}0)_\delta$	$(\bar{1}013)_\alpha$ $// (1\bar{1}0)_\delta$	$(0\bar{1}13)_\alpha$ $// (1\bar{1}0)_\delta$	$(1\bar{1}03)_\alpha$ $// (1\bar{1}0)_\delta$
P-type	$(10\bar{1}0)_\alpha$ $// (1\bar{1}0)_\delta$	$(01\bar{1}0)_\alpha$ $// (1\bar{1}0)_\delta$	$(\bar{1}100)_\alpha$ $// (1\bar{1}0)_\delta$	-	-	-

Table 3 Classification of grains on Surface A and Surface B

Number of grains	Group I			Group II	Total
	B-type	P-type	Total		
Surface A	180	6	186	73	259
Surface B	8	55	63	295	358

Table 4 Deformation gradient tensor of two hydride transitions

	B-type $(10\bar{1}3)_\alpha//(1\bar{1}0)_\delta$	P-type $(10\bar{1}0)_\alpha//(1\bar{1}0)_\delta$
Variant 1	$\begin{bmatrix} 1.055 & 0 & 0.384 \\ 0 & 1.055 & 0 \\ 0 & 0 & 1.086 \end{bmatrix}$	$\begin{bmatrix} 1.218 & 0 & 0 \\ 0 & 1.055 & 0 \\ 0 & 0 & 0.940 \end{bmatrix}$

Table 5 The value *d* of B-type and P-type hydrides in Grain 1, Grain 2 and Grain 3

B-type	Grain 1	Grain 2	Grain 3	P-type	Grain 1	Grain 2	Grain 3
$(10\bar{1}3)_\alpha//(1\bar{1}0)_\delta$	0.667	0.915	0.521	$(10\bar{1}0)_\alpha//(1\bar{1}0)_\delta$	0.725	0.543	0.977
$(01\bar{1}3)_\alpha//(1\bar{1}0)_\delta$	0.862	0.724	0.221	$(01\bar{1}0)_\alpha//(1\bar{1}0)_\delta$	0.366	0.121	0.449
$(\bar{1}103)_\alpha//(1\bar{1}0)_\delta$	0.726	0.973	0.236	$(\bar{1}100)_\alpha//(1\bar{1}0)_\delta$	0.614	0.634	0.468
$(\bar{1}013)_\alpha//(1\bar{1}0)_\delta$	0.413	0.594	0.540				
$(0\bar{1}13)_\alpha//(1\bar{1}0)_\delta$	0.169	0.419	0.804				
$(1\bar{1}03)_\alpha//(1\bar{1}0)_\delta$	0.350	0.641	0.794				

Table 6 The value d of B-type and P-type hydrides in Grain 4 and Grain 5

B-type	Grain 4	Grain 5	P-type	Grain 4	Grain 5
$(10\bar{1}3)_{\alpha}//(1\bar{1}0)_{\delta}$	0.244	0.951	$(10\bar{1}0)_{\alpha}//(1\bar{1}0)_{\delta}$	0.926	0.391
$(01\bar{1}3)_{\alpha}//(1\bar{1}0)_{\delta}$	0.224	0.963	$(01\bar{1}0)_{\alpha}//(1\bar{1}0)_{\delta}$	0.897	0.372
$(\bar{1}103)_{\alpha}//(1\bar{1}0)_{\delta}$	0.270	0.638	$(\bar{1}100)_{\alpha}//(1\bar{1}0)_{\delta}$	0.969	0.978
$(\bar{1}013)_{\alpha}//(1\bar{1}0)_{\delta}$	0.326	0.318			
$(0\bar{1}13)_{\alpha}//(1\bar{1}0)_{\delta}$	0.341	0.307			
$(1\bar{1}03)_{\alpha}//(1\bar{1}0)_{\delta}$	0.304	0.620			

21
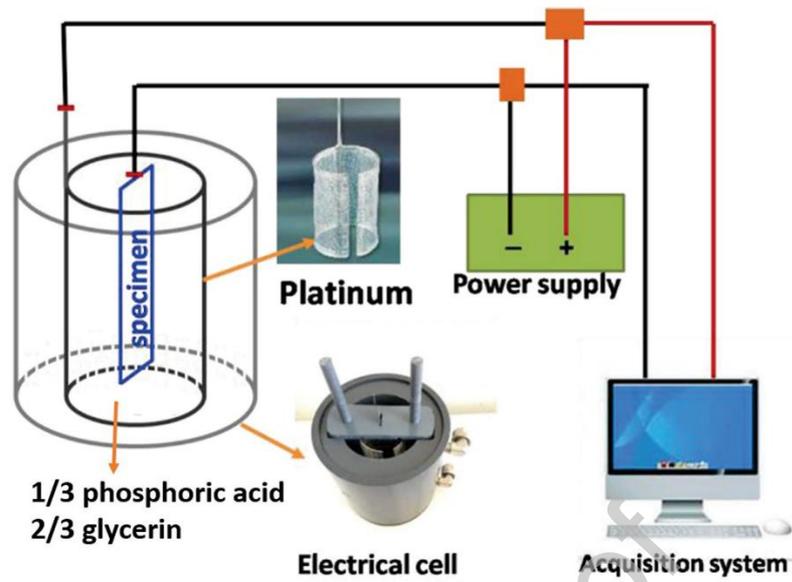
Fig. 1 Schematic presentation of the hydrogen charging system [24]
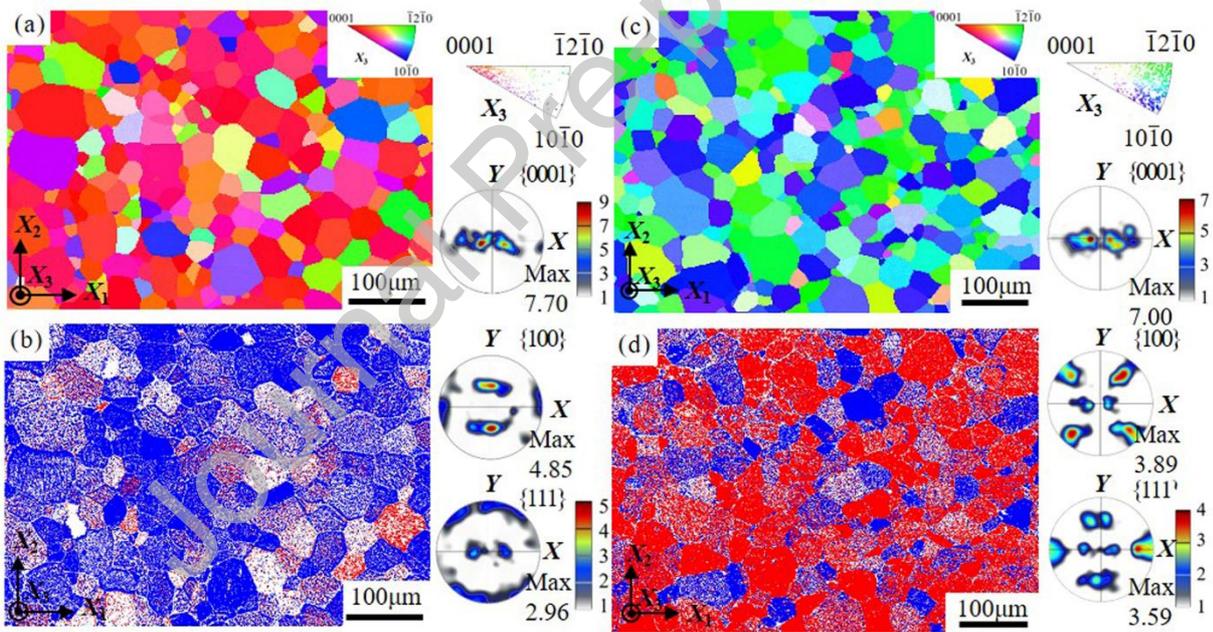
Fig. 2 (a) IPF map of initial grains on Surface A, corresponding IPF and pole figure (b) Phase map of Surface A after hydrogen charging and corresponding pole figures (c) IPF map of initial grains on Surface B, corresponding IPF and pole figure (d) Phase map of Surface B after hydrogen charging and corresponding pole figures (In phase maps, red: α-Ti, blue: δ-hydride, white: zero solution)
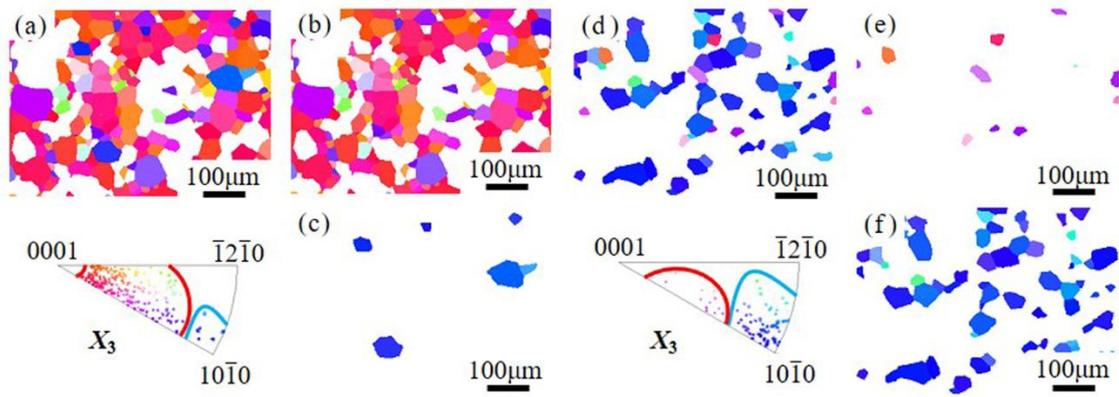
Fig. 3 (a) IPF map of initial Group I grains and corresponding IPF on Surface A (b) IPF map of initial B-type grains on Surface A (c) IPF map of initial P-type grains on Surface A (d) IPF map of initial Group I grains and corresponding IPF on Surface B (e) IPF map of initial B-type grains on Surface B (f) IPF map of initial P-type grains on Surface B
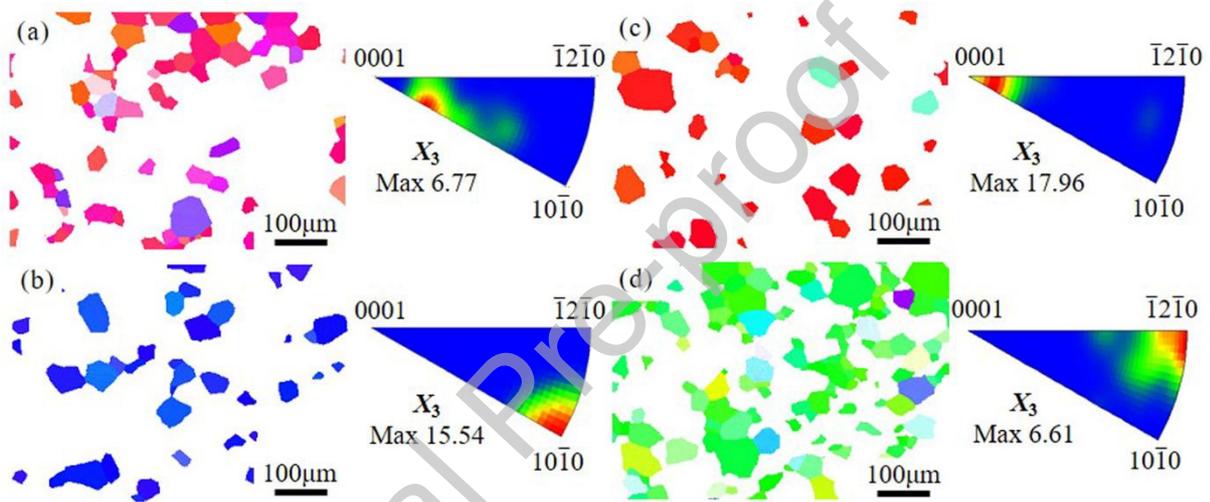

Fig. 4 IPF map of initial grains and corresponding IPF. (a) Grains forming full-covered B-type hydride layer after hydrogen charging (b) Grains forming full-covered P-type hydride layer after hydrogen charging (c) Grains which are non-indexed after hydrogen charging (d) Grains forming few hydrides after hydrogen charging
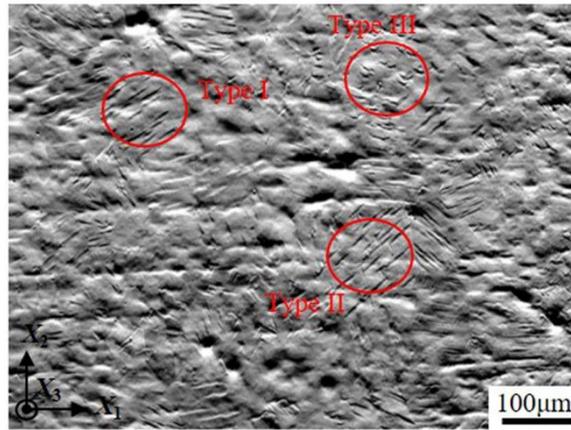
Fig. 5 FSD map of α-Ti matrix with hydride platelets
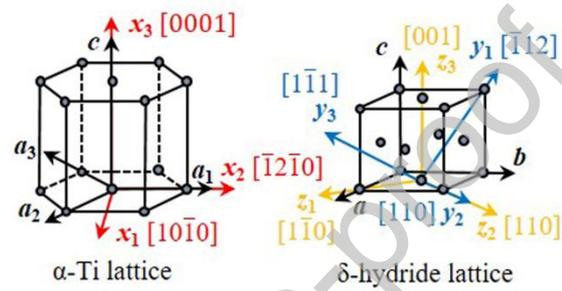
Fig. 6 Crystal coordinate frame of α-Ti (red) and coordinate systems used for α-Ti / δ-hydride transition (blue: B-type hydride, yellow: P-type hydride)
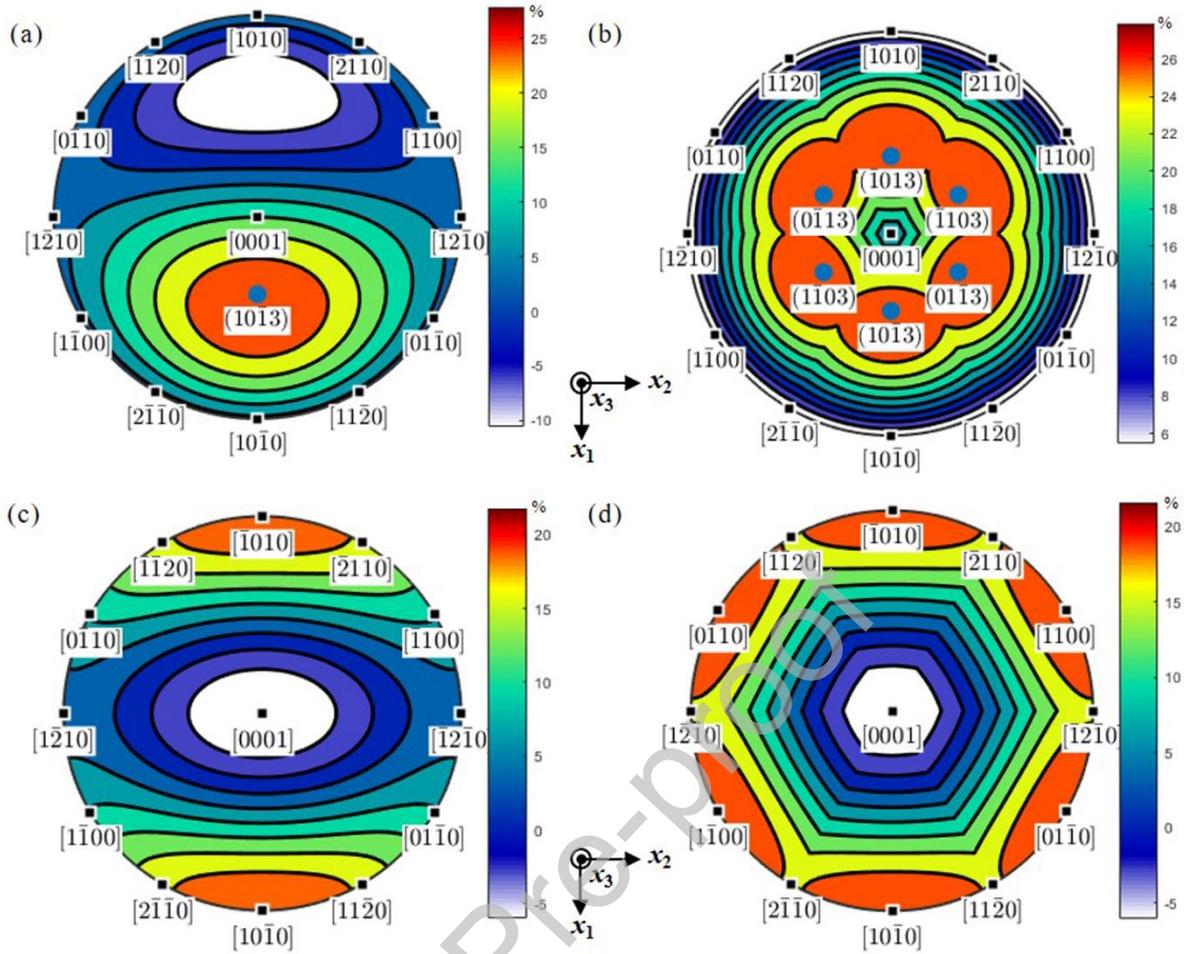
Fig. 7 Full inverse pole figure of strain (a) Variant 1 of B-type hydride (b) Six variants of B-type hydride (c) Variant 1 of P-type hydride (d) Six variants of P-type hydride
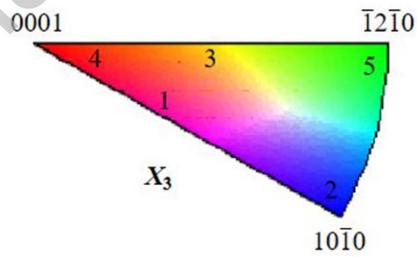
Fig. 8 Positions of five areas in inverse pole figure

25
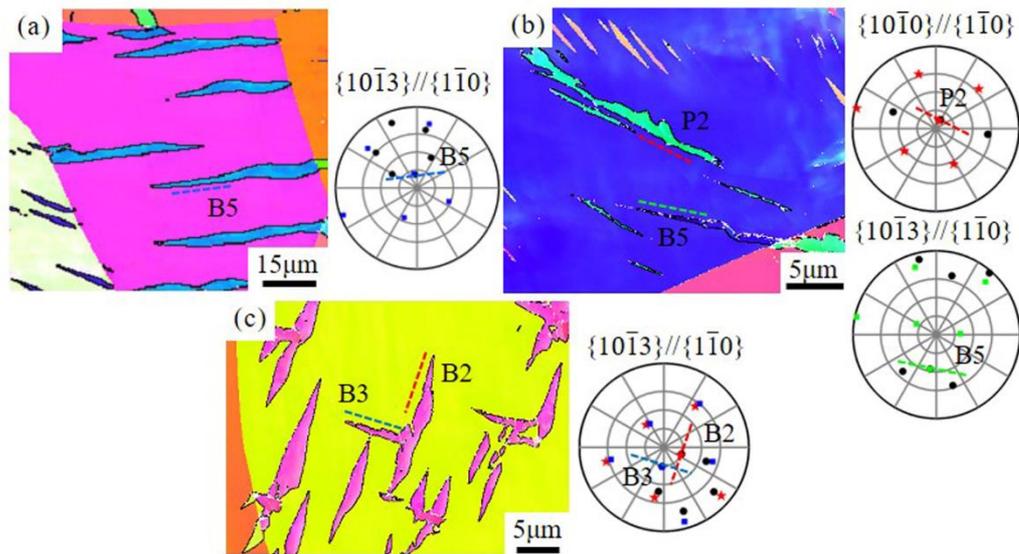
Fig. 9 IPF maps of Group I grains with hydride platelets and corresponding pole figures of hydride interface planes (a) Grain 1, Euler angle: 17.7, 129.8, 23.9 (b) Grain 2, Euler angle: 167.3, 103.2, 34.0 (c) Grain 3, Euler angle: 31.8, 48.9, 1.8. The black dots represent the $\{10\bar{1}3\}$ or $\{10\bar{1}0\}$ interface planes of Ti matrix and the colors represent the $\{1\bar{1}0\}$ interface planes of hydrides. The dotted lines represent the traces of the corresponding hydride interface planes.
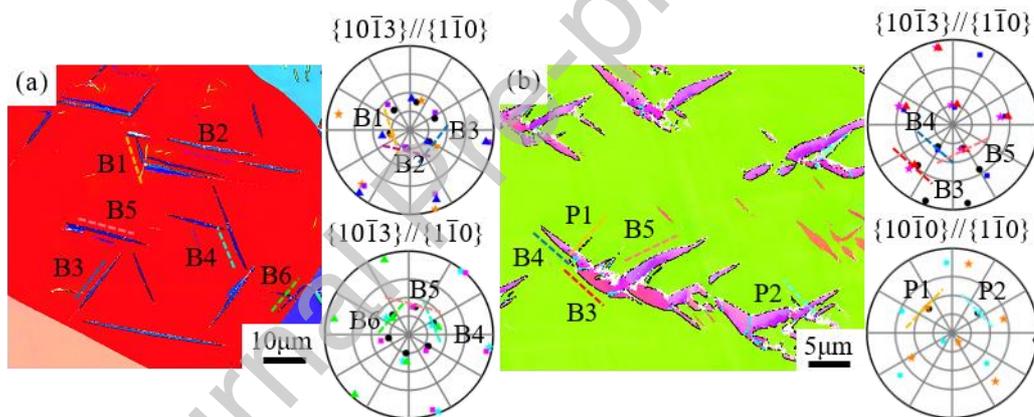

Fig. 10 IPF maps of Group II grains with hydride platelets and corresponding pole figures of hydride interface planes (a) Grain 4, Euler angle: 155.2, 6.4, 43.3 (b) Grain 5, Euler angle: 175.0, 120.5, 58.5. In (b), the blue curves represent the boundaries between hydride variants. In the pole figures of hydride interface planes, the black dots represent the $\{10\bar{1}3\}$ or $\{10\bar{1}0\}$ interface planes of Ti matrix and the colors represent the $\{1\bar{1}0\}$ interface planes of hydrides. The dotted line represents the trace of the corresponding hydride interface planes.